

TiCN coatings deposited by large area filtered arc deposition technique

Y. H. Cheng, T. Browne, and B. Heckerman

Citation: *Journal of Vacuum Science & Technology A* **28**, 431 (2010); doi: 10.1116/1.3372403

View online: <http://dx.doi.org/10.1116/1.3372403>

View Table of Contents: <http://scitation.aip.org/content/avs/journal/jvsta/28/3?ver=pdfcov>

Published by the AVS: Science & Technology of Materials, Interfaces, and Processing

Articles you may be interested in

[Thermally enhanced mechanical properties of arc evaporated Ti 0.34 Al 0.66 N / TiN multilayer coatings](#)
J. Appl. Phys. **108**, 044312 (2010); 10.1063/1.3463422

[Nanocomposite TiSiN coatings deposited by large area filtered arc deposition](#)
J. Vac. Sci. Technol. A **27**, 82 (2009); 10.1116/1.3043460

[Passivation layer on polyimide deposited by combined plasma immersion ion implantation and deposition and cathodic vacuum arc technique](#)
J. Vac. Sci. Technol. A **25**, 411 (2007); 10.1116/1.2712196

[Characterization of \(Ti,Al\)N films deposited by off-plane double bend filtered cathodic vacuum arc](#)
J. Vac. Sci. Technol. A **19**, 557 (2001); 10.1116/1.1351063

[Mechanical properties of titanium nitride coatings deposited by inductively coupled plasma assisted direct current magnetron sputtering](#)
J. Vac. Sci. Technol. A **18**, 524 (2000); 10.1116/1.582219



Instruments for Advanced Science

<p>Contact Hiden Analytical for further details: W www.HidenAnalytical.com E info@hiden.co.uk</p> <p>CLICK TO VIEW our product catalogue</p>	 <p>Gas Analysis</p> <ul style="list-style-type: none"> › dynamic measurement of reaction gas streams › catalysis and thermal analysis › molecular beam studies › dissolved species probes › fermentation, environmental and ecological studies 	 <p>Surface Science</p> <ul style="list-style-type: none"> › UHV TPD › SIMS › end point detection in ion beam etch › elemental imaging - surface mapping 	 <p>Plasma Diagnostics</p> <ul style="list-style-type: none"> › plasma source characterization › etch and deposition process reaction › kinetic studies › analysis of neutral and radical species 	 <p>Vacuum Analysis</p> <ul style="list-style-type: none"> › partial pressure measurement and control of process gases › reactive sputter process control › vacuum diagnostics › vacuum coating process monitoring
--	--	--	--	--

TiCN coatings deposited by large area filtered arc deposition technique

Y. H. Cheng,^{a)} T. Browne, and B. Heckerman

American Eagle Instruments, Inc., 6575 Butler Creek Rd., Missoula, Montana 59808

(Received 28 August 2009; accepted 2 March 2010; published 30 March 2010)

Nanocrystalline TiCN coatings were deposited from Ti targets under the atmosphere of mixed N₂ and CH₄ gases using a novel large area filtered arc deposition technique at a temperature of 350 °C. The microstructure, crystalline structure, bonding structure, coating composition, hardness, modulus, plasticity, and adhesion of the deposited TiCN coatings were systematically characterized using optical microscopy, x-ray diffraction (XRD), x-ray photoelectron spectroscopy, nanoindentation, Rockwell adhesion test, and scratch adhesion test, respectively. By adding 5% CH₄ gas into the chamber, only 2.31 at. % of C was incorporated into the TiN coating to form Ti–C bonds. However, XRD results show a drastic change in the preferred orientation of the TiN grains from strong (111) to strong (220) orientation, as well as a decrease in grain size. Nanoindentation tests indicate a significant increase in hardness and elastic modulus. The plasticity and toughness of the TiCN coatings are comparable to that of the TiN coatings. Adhesion tests show that the TiCN coatings possess excellent adhesion on both 316 and 440a stainless steel substrates. © 2010 American Vacuum Society. [DOI: 10.1116/1.3372403]

I. INTRODUCTION

Transition metal nitrides and carbides are well known ceramic materials because of their high hardness and excellent wear properties. Generally, carbides possess higher hardness, but also higher brittleness as compared with nitrides. By adding C into TiN, a novel hard material, TiCN, which combines the high hardness of TiC and high toughness of TiN, can be formed. TiCN coatings have been used in the industry to improve the wear resistance of the tools and mechanical components due to their high hardness and much improved wear properties.^{1–3} Recently, it was found that TiCN coatings also possess excellent antiadhesive⁴ and antiabrasive⁵ properties.

TiCN coatings have been deposited by magnetron sputtering,^{6,7} cathodic vacuum arc,^{8,9} laser ablation,¹⁰ plasma immersion ion implantation and deposition,¹¹ and chemical vapor deposition (CVD).² CVD was mostly used to deposit TiCN coatings in the cutting tool industry due to the high adhesion of the deposited coatings.² However, the high deposition temperature of the CVD technique limits the selection of base materials because the high deposition temperature, (1000 °C), causes the deformation and softening of the base materials. Cathodic vacuum arc is a promising physical vapor deposition technique for the deposition of well adhered TiCN coatings at low temperature due to their high ionization rate and high ion energy. The major problem for the cathodic arc technique is the macroparticles generated from the evaporation of the target materials, which were codeposited on the substrate surface together with the ions.¹² To remove the unwanted macroparticles, Gorokhovskiy¹³ and Gorokhovskiy *et al.*^{14,15} developed a large area filtered cathodic arc deposition (LAFAD) technique, which utilizes 90° deflecting magnetic fields to deflect ions from the cathodic arc

plasma to the deposition chamber, enabling the deposition of “droplet-free” coatings. By using this technique with a sub-implantation process, we successfully deposit well adhered TiN coatings on dental hand instruments at a low temperature and therefore improve the service life of the instruments five to ten times.

In this study, TiCN coatings were synthesized by using the LAFAD technique from Ti targets under the atmosphere of a mixed 95% N₂ with 5% CH₄ gases. The surface morphology, composition, bonding structure, crystalline structure, hardness, elastic modulus, and adhesion of the deposited coatings were characterized using optical microscopy, x-ray photoelectron spectroscopy (XPS), x-ray diffraction (XRD), nanoindentation, Rockwell adhesion, and scratch adhesion tests.

II. EXPERIMENT

A LAFAD-1 surface engineering system was used to deposit TiCN coatings. The detailed description of the deposition system was previously published.¹⁶ This system consists of one dual filtered arc source, one rectangular plasma-guide chamber, one deposition chamber, auxiliary anodes, heating system, substrate bias system, and vacuum system. The dual filtered arc source consists of two primary cathodic arc sources utilizing round Ti targets, which are placed opposite to each other on the sidewalls of the plasma-guide chamber, surrounded by rectangular deflecting coils, and separated by an anodic baffle plate. The deposition temperature was controlled by heating elements. The deposition zone for this system is about 50 cm diameter × 30 cm high. Mirror finished 17-4, 316, and 440a stainless steel coupons with a size of $\phi 12.5 \times 3$ mm² were used as substrates for characterizing the crystalline structure and mechanical properties of the coatings.

The substrates were ultrasonically cleaned and dried before loading into the deposition chamber. Before deposition,

^{a)}Electronic addresses: yh_cheng@yahoo.com and ycheng@am-eagle.com

the coupons were subjected to Ar plasma cleaning at a pressure, temperature, bias, and time of 0.08 Pa, 350 °C, -250 V, and 15 min, respectively, followed by a Ti ion subimplantation at a pressure, bias, and time of 0.02 Pa, 500 V, and 2 min, respectively. In order to improve the adhesion of the TiCN coatings, a Ti-TiN gradient multilayer with a thickness of about 300 nm was deposited onto the coupon surface. The gradient layer was deposited by gradually increasing N₂ content in the chamber from 0% to 100%. After deposition of the compositional gradient bonding layer, TiCN coatings with a thickness of 2.5 μm were deposited. The TiCN coatings were deposited at a temperature of 350 °C, pressure of 0.02 Pa, substrate bias of -40 V, and CH₄/N₂ flow rate ratio of 5%.

The thickness of the TiCN coatings was measured using a Calo test. The wear scar of the Calo test was used to investigate the cross sectional microstructure of the TiCN coatings. The phase structure and grain size of the TiCN nanocomposite coatings were studied using a Siemens D500 x-ray diffractometer with a Cu K α radiation source ($\lambda = 0.154\ 06\ \text{nm}$). The accelerating voltage and filament current were 40 kV and 30 mA, respectively.

The composition and bonding structure of the TiCN coatings were investigated using a XPS instrument (PHI Model 5600ci, CASA XPS analytical software). A monochromatic Al K α x-ray source was used for all samples. Before XPS measurements, the samples were cleaned using acetone, then were loaded into the ultrahigh vacuum chamber. At first a survey spectrum was acquired. After sputtering with Ar ions for 30 min, another survey spectrum was acquired, followed by acquiring the high-resolution spectra for different elements. The conditions used for the survey scans were as follows: energy range, 1100-0 eV; pass energy, 160 eV; step size, 0.7 eV; sweep time, 180 s; x-ray spot size, 700 × 400 μm². For the high-resolution spectra, an energy range of 40-20 eV was used, depending on the peak being examined, with a pass energy of 10 eV and a step size of 0.05 eV.

Rutherford backscattering (RBS) was also used to characterize the coating composition. For RBS experiment, 1.29 MeV H⁺ ions were used because the cross sections of N and C are enhanced with the H⁺ beam. Ions were incident normal to the sample's surface. Backscattered ions were measured using a Si barrier detector at a scattering angle of 165° and a solid angle of 5.54×10^{-4} sr. The total charge collected for H⁺ spectrum was 120 μC. Spectra were fitted using SIMNRA version 6.02.¹⁷

Nanoindentation tests were conducted using a MTS nanoindenter[®] XP (MTS Systems Corp., Oak Ridge, TN, USA) with a Berkovich diamond tip. Hardness and elastic modulus were measured using the continuous stiffness measurement option. The plasticity of the coatings was characterized by using load-unload displacement curves. Si was used as a standard sample for the initial calibration. The hardness and elastic modulus were obtained from the curves using the Oliver-Pharr method.

The adhesion of the TiCN coating was characterized using the Rockwell C indentation and scratching test methods. For

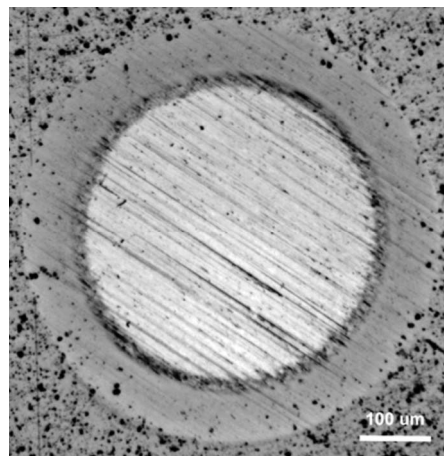


FIG. 1. Optical image of the wear scar of the Calo test on TiCN coating surface.

the Rockwell C indentation test, the size of the diamond tip is 200 μm and the applied load is 150 kg. Three tests were conducted for each sample. Each testing location is separated from the other indent by a minimum of 3 mm. The resulting delamination patterns around the indent were analyzed by optical microscopy. Scratch testing was conducted by a multifunctional scratch tester UMT-2 from CETR. The radius of the indenter is 200 μm. Load rate, scratch speed, and scratch length were set to 100 N/min, 4.5 mm/min, and 8 mm, respectively. Three tests were conducted for each sample. Each testing location is separated from the other indent by a minimum of 2 mm.

III. RESULTS AND DISCUSSIONS

Figure 1 shows the wear scar of the Calo test on TiCN coating surface, which was used to measure the coating thickness. It shows a two layer structure: a 0.3 μm thick bonding layer and a 2.5 μm thick TiCN top layer. A few dark spots were observed in the area close to the surface, indicating the existence of defects in the top layer of the coatings. The rest of the cross section of the TiCN coatings exhibits a dense structure, and no through-coating defects were observed. The composition and bonding structure of the deposited TiCN coatings were characterized by XPS. In order to characterize the composition and the bonding structure of the TiCN coatings, high-resolution spectra of Ti 2*p*, N 1*s*, C 1*s*, and O 1*s* were collected and fitted using a Gaussian function. All spectra were calibrated using the adventitious C 1*s* peak with a fixed value of 284.6 eV. The background from each spectrum was subtracted and the area of under each peak was used to calculate the composition of the TiCN coatings using relative sensitivity factors from the manufacturer's handbook: Ti (1.798), N (0.477), C (0.296), and O (0.711). The atomic content of Ti, N, C, and O was calculated to be 43.38%, 35.97%, 2.31%, and 18.34%, respectively. The coating composition was also measured by RBS, which shows that the TiCN coatings contain 60 at. % Ti, 3.6 at. % C, 33 at. % N, and 3.4 at. % O, providing the considerable oxygen content present in the coatings. The origin of

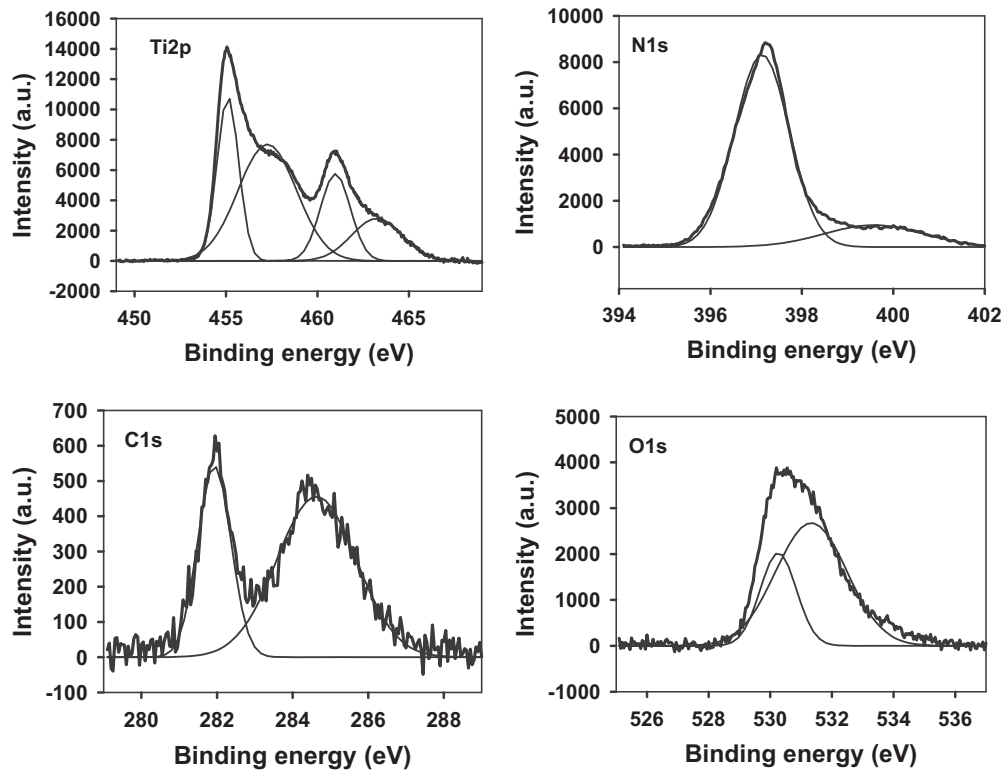


FIG. 2. Deconvolution of the high-resolution Ti $2p$, N $1s$, C $1s$, and O $1s$ XPS spectra of the TiCN coatings.

the measured high oxygen content in the coating results from the following reasons. (1) Surface contamination: As indicated in the first survey spectrum, only two peaks that originated from C and O can be observed, indicating the serious contamination of the coatings surface. The bombardment of the energetic Ar ions can sputter away the contamination, but also can induce the incorporation of O with the TiCN coating surface. (2) The existence of defects in the coatings: As shown in Fig. 1, some defects were observed on the top layer of the coatings. Those defects could trap contaminations containing O, corresponding to the measured high O content.

Figure 2 illustrates the deconvolution results of the high-resolution Ti $2p$, N $1s$, C $1s$, and O $1s$ XPS spectra from the TiCN coatings. As shown, the Ti $2p$ spectrum is characterized by two main peaks at binding energies of 455.0 and 460.9 eV in the binding energy range of 453–467 eV. In addition, two shoulder peaks at binding energies of 457.1 and 463.2 eV are also observed. As a result, four Gaussian functions were used to deconvolute the XPS Ti $2p$ spectra of the TiCN coatings. The first main peak and its shoulder peak are assigned to the $2p_{3/2}$ splitting, and the second main peak and its shoulder peak are their respective $2p_{1/2}$ splitting. According to our previous discussion,¹⁸ the two main peaks correspond to TiN phase, while the two shoulder peaks could be a combination of the intermediate phases, such as TiO₂ or oxynitrides, according to some researchers, as well as the inherent satellite peaks of the two main peaks of the TiN phase.

The N $1s$ XPS spectrum exhibits a nearly symmetric peak at 397.03 eV with a weak shoulder at 399.48 eV in the bind-

ing energy range of 395–402 eV. The binding energy of the main peak is slightly higher than that in the N $1s$ spectra of stoichiometric TiN (396.8 eV). This could be attributed to the synergistic effect of the oxygen, carbon, and titanium atoms in the coatings. The weak shoulder peak is associated with C(*sp*²)–N bond as well as pyridinelike N containing ring.¹⁹ This indicates the existence of N–Ti bonds, N–C bonds, and N–O–Ti bonds in the TiCN coatings, but most of the N atoms in the coating are bonded to Ti atoms.

The C $1s$ spectrum consists of a broad peak and a shoulder peak in the binding energy range of 280–290 eV. The C $1s$ spectra could be fitted well with two peaks at binding energies of 284.6 and 281.8 eV, respectively. The main Gaussian peak is at 284.6 eV with a full width at half maximum (FWHM) of 2.41 eV, which accounts for 79% of the C $1s$ peak area. This peak is assigned to the C–C bonds that originated from the adventitious carbon. The second peak, covering 31% of the peak area, is at 282.1 eV with a FWHM of 0.95 eV, which is very close to the C $1s$ binding energy (281.9 eV) of Ti–C bonds, and can be assigned to the Ti–C bonds.¹¹ This indicates that a small fraction of C atoms is bonded to Ti atoms, and most of the C atoms exist as amorphous carbon. As only the C atoms bonded to Ti affect the coating property, only the area of the shoulder peak was used during the calculation of the coating composition.

The O $1s$ peak exhibits a broad and asymmetric peak in the binding energy range of 529–536 eV. The broad feature indicates the existence of different bondings in the coatings. The O $1s$ peak was fitted with two Gaussian functions cen-

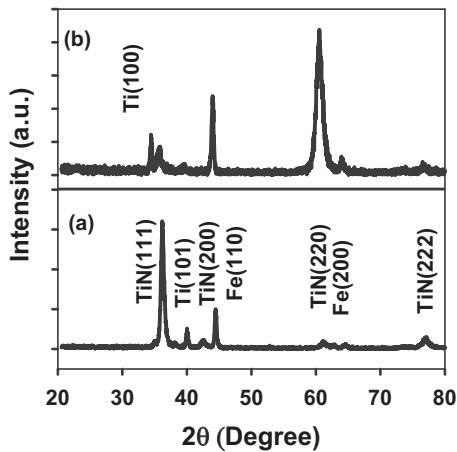


Fig. 3. XRD patterns of the (a) TiN and (b) TiCN coatings on 17-4 stainless steel.

tered at 530.16 and 531.23 eV. The peak at 530.16 eV is assigned to the O–Ti bond in the coatings. It was reported that the binding energy of O^{2-} in TiO_2 coatings is 530.3 eV.²⁰ The binding energy of the peak at 531.23 eV is lower than that of the C–O bond (532.1 eV),⁶ but much higher than that of the O–Ti bonds. This may imply that this peak is attributed to the combined effects of C and Ti atoms to the O atoms, indicating the existence of O–C–Ti bonds in the coating.

The crystalline structure of the TiN and TiCN coatings was investigated by XRD in the 2θ range of 20° – 80° with a θ - 2θ scan. Figure 3 shows the typical XRD patterns of the (a) TiN and (b) TiCN coatings on 17-4 stainless steel substrates. For the TiN coatings, four peaks corresponding to the (111), (200), (220), and (222) planes of the cubic TiN phase appear except for the peaks from the Ti bonding layer and steel substrate. The high intensity of the (111) peak indicates that the deposited TiN coatings exhibit very strong (111) preferred orientation. Compared to the XRD pattern of TiN coatings, one new peak, Ti (100) peak, appears in the XRD pattern of TiCN coatings. In addition, a drastic decrease in the TiN(111) peak intensity and an increase in the TiN (220) peak intensity can be observed, indicating a change in the preferred orientation from (111) to (220).

In order to quantitatively compare the XRD patterns of TiN and TiCN coatings, the TiN (111) peaks were fitted using Gaussian function. The results are shown in Table I. As shown, when compared to TiN coatings, the peak center and full width at half maximum of the TiN (111) peak of the TiCN coatings reduced from 36.23° and 0.49° to 35.70° and 0.66° , respectively. The d values for the TiN (111) plane of

TABLE I. Fitting results of the TiN(111) peak of TiN and TiCN coatings.

	Peak center (deg)	d value (nm)	FWHM (deg)	Grain size (nm)
TiN	36.23	0.2476	0.49	16.9
TiCN	35.70	0.2512	0.66	12.6

TiN coatings and TiCN coatings were calculated using Bragg's law, $1/d_{hkl} = (2/\lambda)\sin\theta$, where d_{hkl} , λ , and θ are interplanar spacing of the (hkl) plane, wavelength of the X-ray, and half of the diffraction angle, respectively. The grain size was computed using the Scherer equation,²¹

$$D = \frac{0.9\lambda}{B \cos \theta}$$

where D is the diameter of the grain, B is the FWHM of the diffraction peak, and θ is half of the diffraction angle. These results are also included in Table I.

From Table I, we see that the d -spacing value of the TiCN coatings is 1.45% larger than that of the TiN coatings. It has been reported that TiCN lattice parameters exhibit values between the TiN and TiC lattice parameters, which are related to the carbon content.²² TiCN coating is a solid solution of TiC and TiN where C(N) atoms substitute N(C) atoms in the lattice. As both compounds are miscible in the entire composition range, no TiC peaks can be detected in the XRD spectrum. In addition, the lattice gradually shifts from TiN to TiC with increasing C content in the coating, corresponding to the increase in the d value of the TiCN coatings. Furthermore, we can see that the grain size in TiCN coatings is slightly smaller than that in TiN coatings.

Nanoindentation was used to investigate the mechanical properties of the TiN and TiCN coatings deposited by LAFAD system. Figure 4 shows the typical (a) hardness and (b) Young's modulus of the TiN and TiCN coatings on 316 stainless steel substrates as a function of the penetration depth of the diamond daps. With increasing penetration depth, all curves increase steeply, then kept at a relatively stable value, followed by a gradual decrease. The initial rapid increase in the measured hardness and Young's modulus has been attributed to the size effect of the diamond tip. The gradual decrease in the measured hardness and Young's modulus at a penetration depth of above 250–500 nm is attributed to the elastic and plastic deformation of the soft substrate under the high load of the indenter.

Clearly, TiCN coatings possess much higher hardness and Young's modulus than TiN coatings. To eliminate the size effect of the diamond tip and the softening effect of substrate, the measured hardness and Young's modulus in the penetration depth of 5%–10% of the coating thickness were averaged and referred as effective hardness and Young's modulus of the coatings. For each coating, ten measurements were performed. The average effective hardness and Young's modulus of the TiN and TiCN coatings were computed to be 33, 376, 39.5, and 406 GPa, respectively.

The load-displacement curve not only provides information about hardness and Young's modulus but also the plasticity and toughness of the hard coatings. Load-displacement measurements at a constant maximum load of 10 mN were conducted on TiN and TiCN coatings. Figure 5 shows the typical load-displacement curves for TiCN and TiN coatings at a maximum load of 10 mN. As shown, at the same maximum load of 10 mN, the maximum displacement of the diamond tip on TiCN coatings (130 nm) is much smaller than

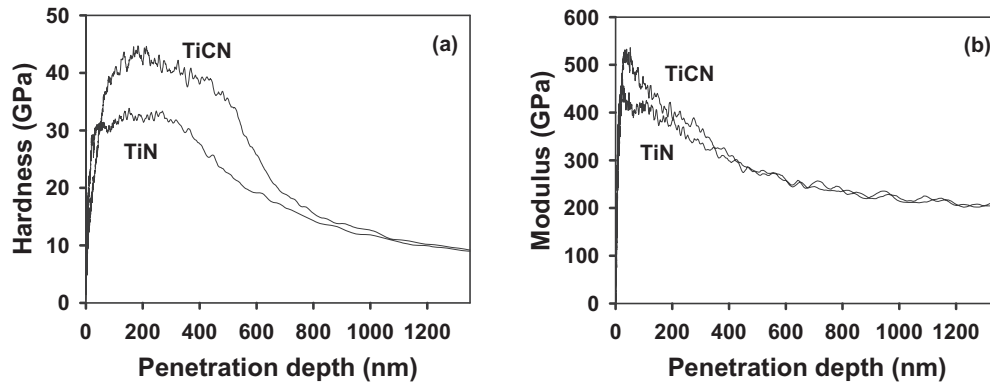


FIG. 4. (a) Hardness and (b) Young's modulus of the TiN and TiCN coatings as a function of the penetration depth of the diamond tip.

that of the TiN coatings (145 nm), indicating the higher hardness and Young's modulus of the TiCN coatings. In addition, the load-displacement curves also provide plastic deformation information of the hard coatings. Plasticity is defined as the ratio of the plastic displacement over the total displacement in the load-displacement curve,²³

$$\text{plasticity} = \frac{\varepsilon_p}{\varepsilon} = \frac{D_r}{D_{\max}}$$

where ε_p is the plastic deformation, ε is the total deformation, D_r is the retained depth of the diamond tip after completely unloading the load, and D_{\max} is the penetration depth of the diamond tip at maximum load. The plasticity of the TiCN and TiN coatings was calculated to be 55% and 59%, respectively. As the toughness is directly correlated with the plastic deformation, generally high plasticity corresponds to high toughness. As TiCN and TiN coatings have similar plasticity, TiCN coatings possess excellent toughness.

The adhesion properties of TiCN coatings on 316 and 440a stainless steels were evaluated using a Rockwell adhesion test and a scratch adhesion test. Rockwell adhesion test is a simple and effective method to evaluate the coating adhesion and was widely used in the coating industry. The adhesion of the coatings can be assigned to HF1-HF6 after comparing the imprint morphologies with the damage patterns. HF1-HF4 guarantees strong interfacial bonds between the coating and the substrate. HF1 is characterized as no

signs of delamination, and the radial of the circumferential cracks is less than 1.5 times of the radius of the indent. HF2 is defined as no signs of delamination, and the radial of circumferential cracks exceeds 1.5 times of the radius of the indent. Figure 6 depicts the 40 \times optical images of Rockwell indenter imprint on TiCN coatings on (a) 316 stainless steel and (b) 440a stainless steel substrates. The piling up of the steel at the edge of the imprints was observed on all the samples in the low magnification images. This is typical for Rockwell testing on soft substrates. Due to the low hardness of the 316 stainless steel when compared to the 440a stainless steel, the imprints on the 316 coupons are much larger. The deformation of the substrate generates high shear stress in the interface of coatings and substrate, leading to the formation of circumferential cracks on the TiCN coatings deposited on 316 stainless steel substrates. The maximum radius of the circumferential cracks is about two times the radius of the indent, indicating that the adhesion of the coating belongs to class HF2. The radius of the circumferential cracks on the coating on 440a substrates is much smaller (<1.5 times of the radius of the indent), indicating that the adhesion of the coating on 440a substrate belongs to HF1. The Rockwell adhesion results imply that TiCN coatings exhibit excellent adhesion on both 316 and 440a stainless steel substrates.

Figure 7 illustrates the scratch adhesion test results of the TiCN coatings on (a) 316 stainless steel and (b) 440a stain-

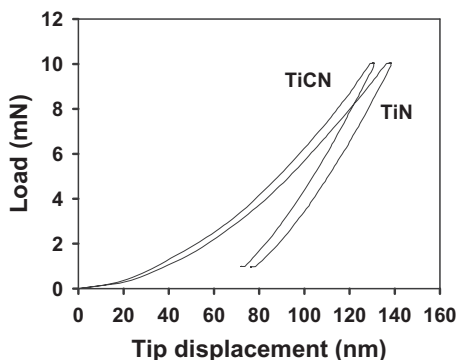


FIG. 5. Load-displacement curves of TiN and TiCN coatings deposited by LAFAD.

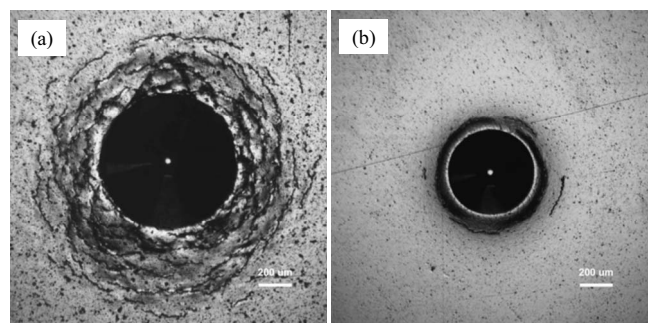


FIG. 6. Morphology of the imprint of the diamond tip on TiCN coatings on (a) 316 stainless steel and (b) 440a stainless steel after Rockwell adhesion test.

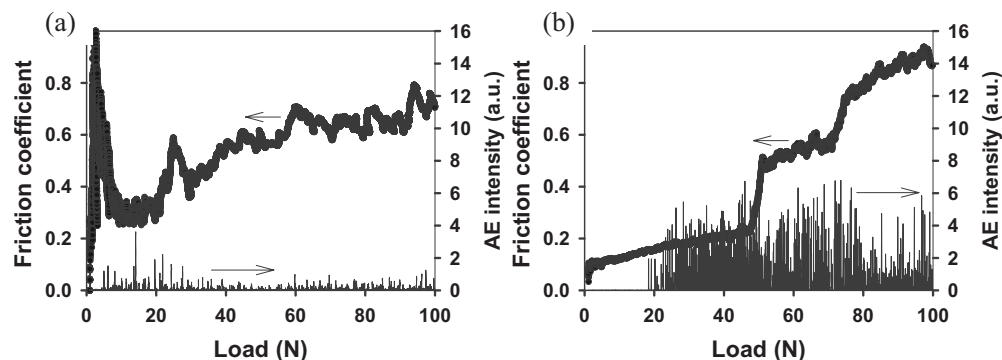


Fig. 7. Scratch test results of the TiCN coatings on (a) 316 stainless steel and (b) 440a stainless steel substrates.

less steel substrates. Figure 7(a) shows that the friction coefficient curve is very rough, which increases gradually with increasing load after passing the initial spike. Optical microscopy observation shows that the coatings were not completely removed even at a load of 100 N, indicating the excellent adhesion of the TiCN coatings on the 316 stainless steel substrates. The acoustic emission (AE) signal intensity is very low and the signal starts to appear at a load of 5 N, corresponding to the critical load that cracks starts (Lc1).

The friction coefficient and AE intensity versus load curves measured for TiCN coatings on 440a substrates are significantly different. The friction coefficient increases linearly with increasing load, then rapidly increases at a load of about 50 N, followed by a gradual increase with the further increase in the applied load. After comparing using the optical microscopy results, it was found that the rapid increase in the friction coefficient results from the complete removal of the coating from the 440a substrate. This load corresponds to the critical load Lc2. In addition, the AE signal is very strong and starts to appear at a load of 19 N, indicating that the measured Lc1 is 19 N.

As discussed above, both Rockwell adhesion and scratch adhesion test results demonstrate that the Ti/TiN/TiCN multilayer coatings have excellent adhesion on both 316 and 440a stainless steel substrates. However, it is interesting to note that the Rockwell tests reveal that the multilayer coatings have a better adhesion on 440a substrate, and the scratch tests show that the coatings on 440a substrate have higher Lc1 value, but lower Lc2 value. This discrepancy results from the big difference in the mechanical properties of the 316 and 440a stainless steels. It is well known that 440a stainless steel has much higher hardness and much lower toughness than that of the 316 stainless steel. During the scratch tests, the movement of the diamond tip at high load leads to the plastic deformation of the 316 stainless steel. Due to the high adhesion, the coatings still adhere on the seriously deformed 316 stainless steel. However, for 440a stainless steel, the movement of the diamond tip causes the removal of the coatings together with the top layer of the 440a substrate due to the brittle nature of the 440a stainless steel. As a result, it is impossible to tell when the coatings were detached from the 440a substrate.

IV. CONCLUSIONS

In this study, the LAFAD deposition technique was used to deposit TiCN coatings from Ti target under the atmosphere of a mixed 95% N₂ and 5% CH₄ gases. Optical microscopy observation shows that the deposition TiCN coatings are dense and there are no through-coating defects along the cross section of the coatings. XPS results indicate that Ti–N, Ti–C, Ti–O, C–N, and Ti–O–C bonds exist in the coatings and the carbon content in the coatings is 2.31 at. %. XRD results indicate that the TiCN coatings exhibit a face centered cubic structure with a complete (220) preferred orientation and have smaller grain size than TiN coatings. Nanoindentation results show that the TiCN coatings possess higher hardness (39 GPa) and Young's modulus (406 GPa) than that of the TiN coatings (33 and 379 GPa, respectively), as well as comparable plasticity and toughness to TiN coatings. Both Rockwell and scratch adhesion tests demonstrate that the TiCN coatings possess excellent adhesion on both 316 and 440a stainless steel substrates.

ACKNOWLEDGMENTS

The authors would like to express their gratitude for the support of The United States Army Telemedicine and Advanced Technology Research Center (TATRC) and the U.S. Army Medical Research and Materiel Command under Contract No. W81XWH-08-2-0023.

¹E. Ertürk, O. Knotek, W. Bergmer, and H. G. Prengel, *Surf. Coat. Technol.* **46**, 39 (1991).

²A. Larsson and S. Rупpi, *Thin Solid Films* **402**, 203 (2002).

³J. Walkowicz, J. Smolik, K. Miernik, and J. Bujak, *Surf. Coat. Technol.* **81**, 201 (1996).

⁴F. J. Teeter, *Ceramic Coating* (ASME, New York, 1993), Vol. 44.

⁵E. Bergmann, H. Kaufmann, R. Schmid, and J. Vogel, *Surf. Coat. Technol.* **42**, 237 (1990).

⁶L. C. Agudelo, R. Ospina, H. A. Castillo, and A. Devia, *Phys. Scr.* **T131**, 014006 (2008).

⁷L. F. Senna, C. A. Achete, T. Hirsch, and F. L. Freire, Jr., *Surf. Coat. Technol.* **94–95**, 390 (1997).

⁸L. Karlsson, L. Hultman, and J. E. Sundgren, *Thin Solid Films* **371**, 167 (2000).

⁹Y. Y. Guu and J. F. Lin, *Wear* **210**, 245 (1997).

¹⁰J. M. Lackner, W. Waldhauser, and R. Ebner, *Surf. Coat. Technol.* **188–189**, 519 (2004).

¹¹Y. Cheng and Y. F. Zheng, *Surf. Coat. Technol.* **201**, 4909 (2007).

- ¹²R. L. Boxman, D. M. Sanders, P. J. Martin, and J. M. Lafferty, *Handbook of Vacuum Arc Science and Technology: Fundamentals and Applications* (Noyes, Park Ridge, NJ, 1995).
- ¹³V. Gorokhovskiy, U.S. Patent No. 6,663,755 B2 (2003).
- ¹⁴V. I. Gorokhovskiy, D. G. Bhat, and R. Bhattacharya, *Surf. Coat. Technol.* **140**, 215 (2001).
- ¹⁵Vladimir Gorokhovskiy, Chris Bowman, Paul Gannon, Dave VanVorous, Andrey Voevodin, and A. Rutkowski, *Surf. Coat. Technol.* **201**, 6228 (2007).
- ¹⁶Y. H. Cheng, T. Browne, B. Heckman, J. C. Jiang, E. I. Meletis, C. Bowman, and V. Gorokhovskiy, *J. Appl. Phys.* **104**, 093502 (2008).
- ¹⁷See: <http://www.rzg.mpg.de/~mam/>.
- ¹⁸Y. H. Cheng, T. Browne, and B. Heckman, *J. Vac. Sci. Technol. A* **27**, 82 (2009).
- ¹⁹S. Meskinis, M. Andrulevicius, V. Kopustinskas, and S. Tamulevicius, *Appl. Surf. Sci.* **249**, 295 (2005).
- ²⁰Z. Niu, X. Jia, W. Zhang, W. Chen, and K. Qian, *Appl. Surf. Sci.* **252**, 2259 (2006).
- ²¹L. V. Azaroff, *Elements of X-ray Crystallography* (McGraw-Hill, New York, 1968).
- ²²L. F. Sienna, C. A. Achete, T. Hirsch, and O. Mattos, *Surf. Eng.* **21**, 144 (2005).
- ²³S. Zhang, D. Sun, Y. Fu, and H. Du, *Surf. Coat. Technol.* **198**, 74 (2005).